JOURNAL OF AGRICULTURAL AND FOOD CHEMISTRY

Article

pubs.acs.org/JAFC

In Situ Imaging Highlights Local Structural Changes during Heating: The Case of Meat

Mustapha Bouhrara, Sylvie Clerjon,* Jean-Louis Damez, Alain Kondjoyan, and Jean-Marie Bonny

INRA, UR370 Qualité des Produits Animaux F-63122 Saint-Genès-Champanelle, France

ABSTRACT: Understanding and monitoring deformation and water content changes in meat during cooking is of prime importance. We show the possibilities offered by nuclear magnetic resonance imaging (MRI) for the in situ dynamic measurement of deformation fields and water content mapping during beef heating from 20 to 75 °C. MRIs were acquired during heating, and image registration was used to calculate the deformation field. The temperature distribution in the sample was simulated numerically to link structural modifications and water transfer to temperature values. During heating, proton density decreases because of a magnetic susceptibility drop with temperature and water expulsion due to muscle contraction. A positive relationship was found between local cumulative deformation and water content. This new approach makes it possible to identify the deformation field and water transfer simultaneously and to trace thermal history to build heuristic models linking these parameters.

KEYWORDS: *meat, heating, dynamic MRI, deformation fields, cooking loss, structure*

INTRODUCTION

Control of the sensory, nutritional, and technological qualities of end products is of prime importance for both consumers and industry. The case of meat is of particular interest because of the high sensitivity of its palatability traits to heating processes. The stakes are high for industrial companies that have to manage the cooking process of an increasing range of meat products.

Juice loss (also called water loss because it contains only 5−10% of dry matter) is a major palatability trait emphasized by consumers, which has to be monitored and controlled by the meat industry to ensure more efficient marketing of muscles and muscle groups.[1] Furthermore, juiciness has been reported to be correlated with tenderness, the main palatability trait,[2,3] but with low correlation as reported by Dransfield et al.[4] Indeed, water loss leads to lower perceived toughness, as the juices act as a sort of lubricant during mastication.[5] In particular, higher juiciness plays a crucial role in acceptance of meat by young and elderly people, leading to longer mastication time of the bolus and in turn leading to better assimilation of nutrients.[6]

Water losses are induced by structural changes that occur in meat during cooking.[7] Classically, cooking loss is measured by weighing the samples before and after heat treatment and expressed as a percentage of the original weight. The reference method for obtaining this parameter was well-described by Honikel.[8] An improvement of this reference method is to collect and weigh the water in real time during the heating process.[9] Moreover, the latter authors measured the electrical conductivity of juice during cooking. With this technique, it is possible to correlate cooking loss and protein denaturation. Indirect, contactless methods of measuring water content after cooking have been developed. By using meat color measurement, Zheng[10] showed good correlation between moisture content and color features after cooking beef *triceps brachii* pieces cooked in a water-bath until their core temperature reached 72 °C. The result subjected to image analysis[11] showed that the cooking shrinkage of the surface area and volume was significantly correlated with cooking loss. In addition to the simple measurement of cooking loss, magnetic resonance imaging (MRI) makes it possible to monitor water transfer dynamically and locally during processes. It has been applied for wheat kernels drying,[12] the rehydration of extruded pasta,[13] the drying of a food gelatin analogue,[14] and the rehydration of rice grains[15] during cooking. However, to our knowledge, it has never been applied during meat heating.

MRI is a nondestructive imaging method adapted to in situ and local analysis. Applied to meat during heating, it opens new paths for observing detailed changes in muscle structure and internal water transfer simultaneously. It requires prior methodological adjustments in order to apply a controlled thermal constraint to a sample in the high-field MRI magnet and acquire images from which deformation and water content can be derived with time. To achieve this, we introduced a novel MRI-compatible device, which heats the sample via a fluid, and a strategy based on the dynamic acquisition of images showing the contrast between muscle fibers and intramuscular connective tissue.[16] Tracking these fiducial markers allowed reconstructing the required deformation maps.[17] By using an additional validated simulation method, which provided temperature in the sample with time, the relationship between deformation and temperature was measured in different regions of the sample and was then averaged in a model. The underlying mechanisms of the three deformation phases, highlighted globally, were elucidated on the basis of the known behaviors of thermally sensitive muscle compounds (i.e., myosin, collagen, and sarcoplasmic proteins).

Finally, the water is expelled by the formation of intermyofibrilar channels between the fiber bundles followed by a

Received: November 16, 2011
Revised: March 27, 2012
Accepted: April 2, 2012
Published: April 2, 2012

dx.doi.org/10.1021/jf2046569 | J. Agric. Food Chem. 2012, 60, 4678−4687

global deformation of the meat.[18,5] The pertinence of the approach followed by these works leads us to continue these qualitative observations and map the water content in meat during heating and then investigate the quantitative relationship between temperature, deformation, and water content. Nevertheless, simultaneous mapping of deformation and water content requires major developments in MRI to acquire images rapidly enough to monitor the fast structural changes and water transfer occurring in muscles, especially at high critical temperatures. A second key aim is to map water content (i.e., proton spin density, PD) by taking the main source of bias into account, i.e., the variations of amplitude B1 of the active emission radiofrequency (RF) field (pulsed during the MRI experiments) with temperature.

In this article, we present our results quantifying temperature, deformation, and water content during a meat heating process. Advantage was taken of in situ imaging to obtain local and simultaneous assessment for the first time. It is organized as followed: (i) we provide a brief description of the experimental hardware and meat samples; (ii) a description is then given of the MRI methods developed and used to solve the issues introduced before, by focusing on the approach used for accelerating the MRI acquisition process and mapping both deformation and PD; (iii) finally, the interactions between parameters is presented and discussed in view to understanding the mechanisms linking temperature, deformation, and water content during meat heating.

MATERIALS AND METHODS

Samples and Hardware. *Biceps femoris* (BF) coming from Charolais cow samples were cut in the form of cylinders 5 cm in diameter by 6 cm in length, with the muscle fibers oriented axially. We chose this muscle because its richness in elastin is visible by T_2*-weighted MRI. The dimensions of the sample were chosen to obtain an adequate picture of the perimysial structure of the muscle and still fit the dimensions of the MR imager. The meat cylinders were then placed in plastic bags in a vacuum to prevent direct contact with the circulating heating water. The results presented here were obtained from four samples: two samples from the same first animal containing high IMCT (intramuscular connective tissue) (high IMCT content 1 and high IMCT content 2), and the two others from a second animal containing low IMCT (low IMCT content 1 and low IMCT content 2). This rating according to IMCT content was based on visual observation. For each sample, our analyses were performed on five transverse slices, which intercepted the muscle fiber axis perpendicularly.

Each sample was heated over the temperature range 20−75 °C using water circulating (42 L/min) in an MRI-compatible device. It comprised a watertight sample holder cell made of polyetheretherketone placed inside a Teflon sleeve to ensure thermal insulation between the cell and the RF coil. The regulation system was programmed so that the temperature of the water rose constantly at a gradient of 0.63 °C/min. This low gradient (regarding those commonly applied in industrial processes) was chosen for being compatible with our MRI acquisition times.

Image acquisition was carried out using a Biospec horizontal 4.7 T MRI system (Bruker GmbH, Ettlingen, Germany), with a 26 cm diameter bore, equipped with a BGA-26 rapid gradient system, and using a linear polarized birdcage coil for both emission and reception. The main fiber axis in the sample was placed approximately parallel to the direction of the static magnetic field of the magnet. The heating water runoff was roughly directed by the pump installed parallel to this direction.

Temperature Mapping. Temperature maps were obtained from numerical simulations with finite elements using the Comsol Multiphysics 3.4 software. The heat exchanges in the juice and the meat were considered as purely conductive. Water flow inside the sample was neglected because it was checked by simulations for having a very low influence in the heat exchanges. The calculation was performed stepwise on the basis of the areas occupied by the meat after shrinkage and by the expelled juice, respectively. These areas were determined at each step by manual segmentation of MR images, which clearly delineated the juice−meat interface throughout the heating process. This approach was described in more detail and compared in ref 16 with invasive measurements, which demonstrated a maximum error of between 0.5 and 1 °C.

Dynamic MRI for Deformation and Proton Density Mapping. The imaging protocol consisted in continuous acquisition during heating of the same block made up of four different image sets. These sets were designed to acquire the images needed for accurate and fast quantitative mapping of deformation and PD.

The first set of images, named deformation images (DI), was acquired for highlighting the contrast between muscle fibers and intramuscular connective tissue. To do this, T_2*-weighted images sensitive to differences of the magnetic susceptibility produced by the fiber-connective tissue interfaces inside the muscle were required. The protocol described in ref 17 for mapping only deformation was perfected in order to accelerate image acquisition, the objective being to keep a reasonable delay between two successive T_2*-weighted data sets because part of the time was spent acquiring the images needed for PD mapping. To this end, three gradient-echoes (GE) were acquired instead of a single echo during each repetition time (TR). We used centric encoding to maximize the signal-to-noise ratio (SNR) and minimize artifacts due to static field inhomogeneities. This approach was combined with half *k*-space sampling,[19] a dedicated algorithm (POCS)[20] used for reconstructing images free of artifacts due to the missing part of *k*-space. The other image parameters were TR = 2 s, effective TE = 13 ms, FOV = 54 × 54 mm^2, matrix = 216 × 216, and slice thickness = 2 mm (volume of the resulting voxel 0.25 × 0.25 × 2 mm^3). Multiple-GE and partial-sampling strategies led to an acceleration by 3 and 1.6, respectively, with an acquisition time of (2″ × 216)/(3 × 1.6) = 1′30″.

The acquisition of second and third sets of images, named PD images (PDI_1 and PDI_2), was necessary for PD mapping. It consisted in two spin−echo (SE) acquisitions of the same slices differing only by their echo times (i.e., TE_1 = 13 ms and TE_2 = 51 ms, respectively). Since a long TR was necessary for mitigating T_1 dependence liable to bias PD maps, segmented echo planar encoding was used for accelerating PDI acquisition. This was logical because SE-EPI is much less prone to susceptibility artifacts than GE-EPI and is well-adapted for quantitative mapping of PD at low spatial resolution,[21] as such resolution is sufficient for steady variation of water content in the muscle. The other image parameters were TR = 6 s, FOV = 54 × 54 mm^2, matrix = 108 × 108, slice thickness = 2 mm (volume of the resulting voxel 0.5 × 0.5 × 2 mm^3), and flip angles = 64°/180°. The use of segmented EPI led to an acceleration by a factor of 4 with the acquisition time being (6″ × 108)/4 = 2′42″ per PDI.

The last set of images was acquired for measuring amplitude B1 of the active emission RF field. In the high field (here, 4.7 T), the interactions between this emission RF field and the (muscle) sample caused inhomogeneity of B1, which was no longer negligible. Indeed, this inhomogeneity causes undesired effects during both spin excitation and signal reception, biasing the determination of PD when using the procedure described in the previous paragraph. B1 distribution results from complex interference between decaying magnetic waves traveling in the sample-coil set and near fields induced by reflections at the interfaces (i.e., muscle, plastic bag, water, device, air, and coil). Equally important, the electromagnetic properties of the muscle evolve during heating because permittivity (encompassing conductivity and dielectric constant) increases with both temperature and water content.[22,23] Sample shrinkage during heating modifies the coupling between the sample and the RF coil.[17,24,25] Since B1 distribution depends on these unknown and evolving factors, experimental mapping of B1 was preferred to numerical simulations and was done along with the acquisition of PDI_1 and PDI_2, to obtain adequate correction of PD maps during heating. The protocol for measuring B1 distribution was an extension of the reference double-angle method,[26] which achieved high-precision and fast B1-mapping

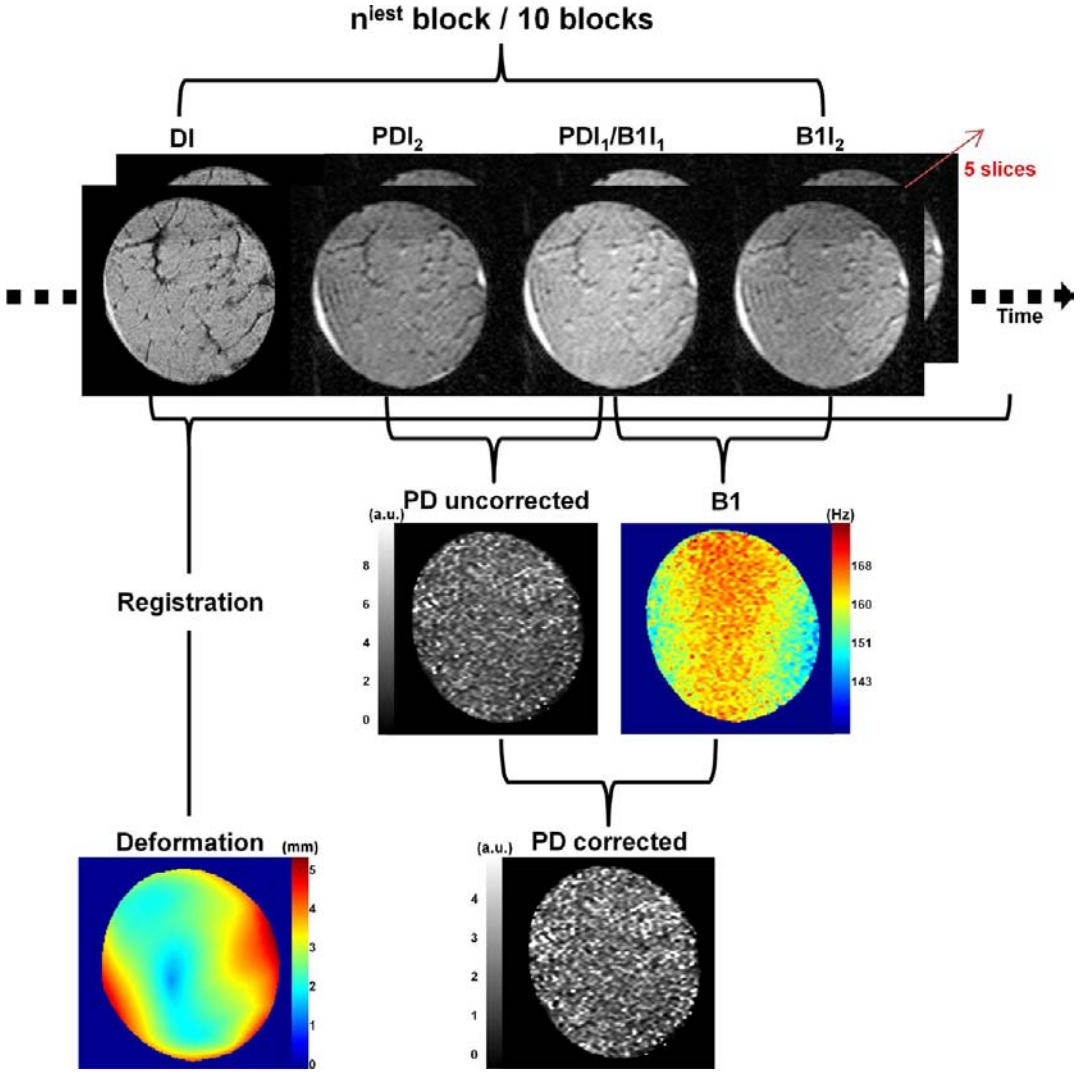

Figure 1. Schematic representation of deformation and water content mapping during heating by dynamic MRI.

using two SE images.[27] It used PDI_1 obtained with an excitation flip angle of 64° and a second one differing only by its excitation flip angle of 127°. Note that these two images are named B1 images ($B1I_1$ and $B1I_2$, respectively) and that PDI_1 and $B1I_1$ denominate the same image.

DI, PDI_1/ $B1I_1$, PDI_2, and $B1I_2$ were obtained in the same 5 slices spaced at 4 mm, oriented in the transverse plane to intercept the muscle fiber axis perpendicularly. The total acquisition time for the 4 image sets was (1′30″ + (3 × 2′42″)) = 9′36″. It was repeated 10 times during the temperature increase of the heating water between 20 and 75 °C (0.63 °C/min).

Reconstruction of Deformation and Proton Density Maps. The first step was to reconstruct the deformation fields of the sample from two successively acquired DIs. The deformation field at temperature t_i is the geometrical transformation required to pass from the image obtained at temperature t_{i-1} to that obtained at temperature t_i. We demonstrated previously that a 2D fourth order polynomial spatial transformation is adequate for modeling muscle deformation during heating.[17] Then, the degrees-of-freedom of this transformation were estimated by minimizing the difference between the two DIs using an automated image registration package.[28,29] This registration is possible provided that the internal fiducial markers appear in the DIs throughout the heating process. Finally, the deformation field $\mathbf{W}(t_i)$ was inferred by computing the two components of 2D displacement in each voxel position of the image.

Using the two PDIs acquired at temperature t_i, the uncorrected PD was computed voxelwise according to

$$\widehat{PD}(t_i) = PDI_1 \exp\left(\frac{TE_1}{\hat{T}_2}\right) \quad ([1])$$

where $\hat{T}_2$ was estimated assuming a monoexponential behavior of T_2 decays, i.e.,

$$\hat{T}_2(t_i) = \frac{(TE_2 - TE_1)}{\ln\left(\frac{PDI_1}{PDI_2}\right)} \quad ([2])$$

B1-maps were reconstructed from the two SE images, $B1I_1$ and $B1I_2$ according to the method described in our previous work.[27] The effects of B1 inhomogeneities were integrated in a single spatially varying correction factor assuming reciprocity; i.e., since the same coil was used for emission and reception, reception sensitivity was proportional to the amplitude of the emission field. Finally, corrected PD was obtained by dividing $\widehat{PD}(t_i)$ by this correction factor.

The whole approach for image acquisition and reconstructing quantitative maps is shown in Figure 1.

From Local Information to Average Behaviors. The specific evolution of temperature was known locally and as a function of time. It was therefore possible to link the deformation and proton density time-courses measured in a given voxel from the maps, to their temperature rates. Our general approach was then to average such

dx.doi.org/10.1021/jf2046569 | J. Agric. Food Chem. 2012, 60, 4678–4687

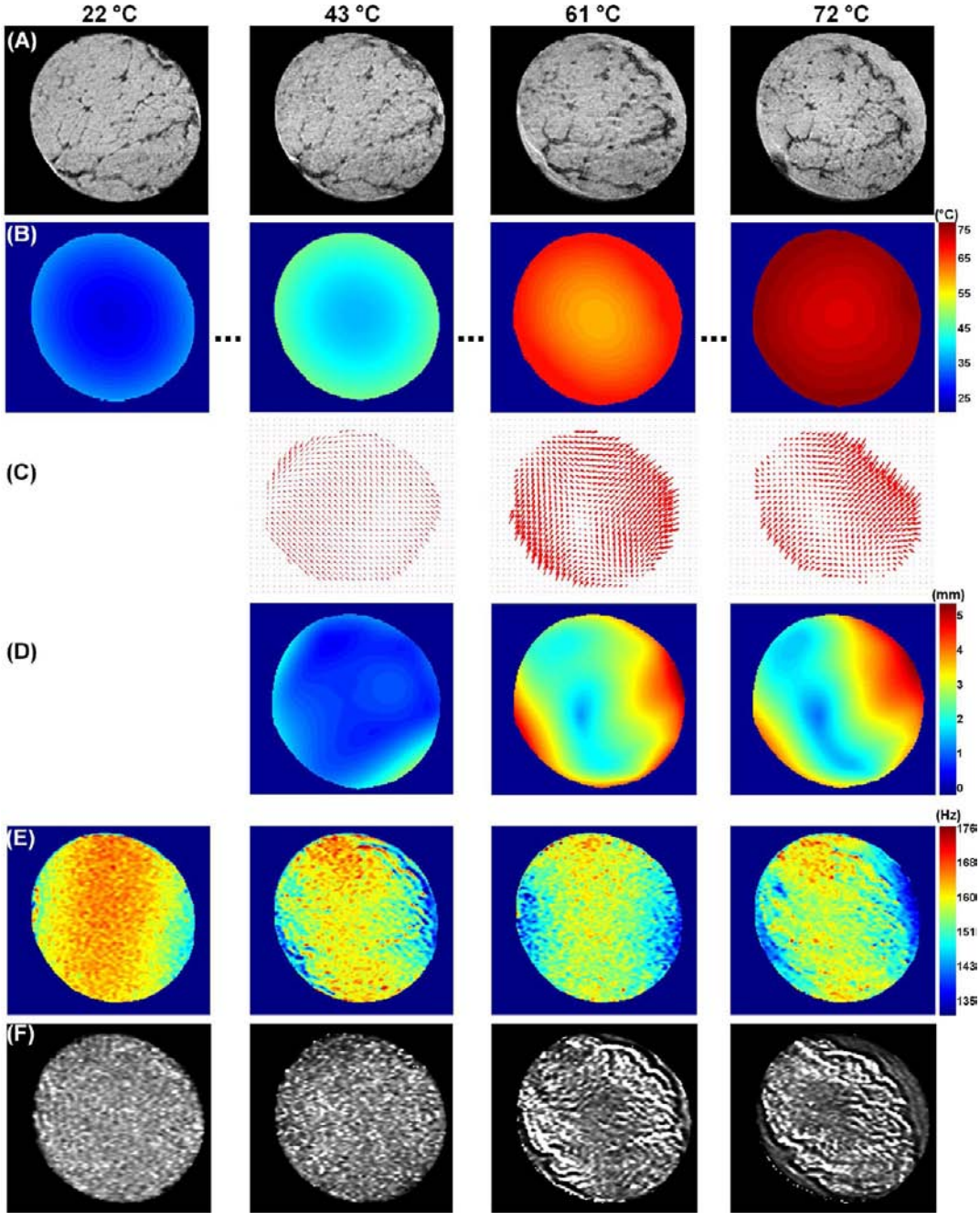

Figure 2. Sample with high IMCT content (slice 3/5). (A) T_2*-weighted MR images (DIs). The windowing of gray levels was adjusted for each image to compensate for continuous SNR loss. (B) Corresponding temperature maps obtained by numerical simulation for four average temperatures in the sample. (C) Corresponding representations of deformation as a function of direction and magnitude calculated by nonlinear optimal registration from two consecutive DIs. (D) Corresponding representations of the magnitude of deformation calculated by nonlinear optimal registration from two consecutive DIs. (E) Corresponding B1 maps. (F) Corresponding proton density maps.

local relationships for all the voxels of the images in order to highlight general laws.

Each voxel of the image obtained at 20 °C was tracked by successively applying the transformation $\mathbf{W}(t_i)$. Deformation, PD, and temperature were collected from the quantitative maps along this trajectory as a function of time t_i. From an application point of view, it is interesting to know the impact of temperature on the final deformation; this corresponds to the accumulation of deformations between two successive images. Cumulative deformation and PD time-courses were placed in a common space where temperature became the abscissa. Lastly, these temperature-courses were averaged over all the voxels of the slice. All our samples were heated from 20 to 75 °C. Despite this, at the end of cooking, few voxels had effectively reached 75 °C. Thus, to ensure robustness, the average models were only defined up to 70 °C.

In order to quantify the correlation between the PD and the cumulative deformation, several regions of interest (ROI) were defined manually for each of the 5 slices of each sample and for the last two images of our acquisition series, presenting the highest average temperatures (~70 °C). We chose to work on these images of the end of the process on which cumulative deformation and PD were most visible. For the ROI, a homogeneous deformation zone was chosen, and the average cumulative deformation and the corresponding PD in this ROI were calculated.

All the numerical procedures were performed with Matlab (MathWorks Inc., Natick, USA).

dx.doi.org/10.1021/jf2046569 | J. Agric. Food Chem. 2012, 60, 4678–4687

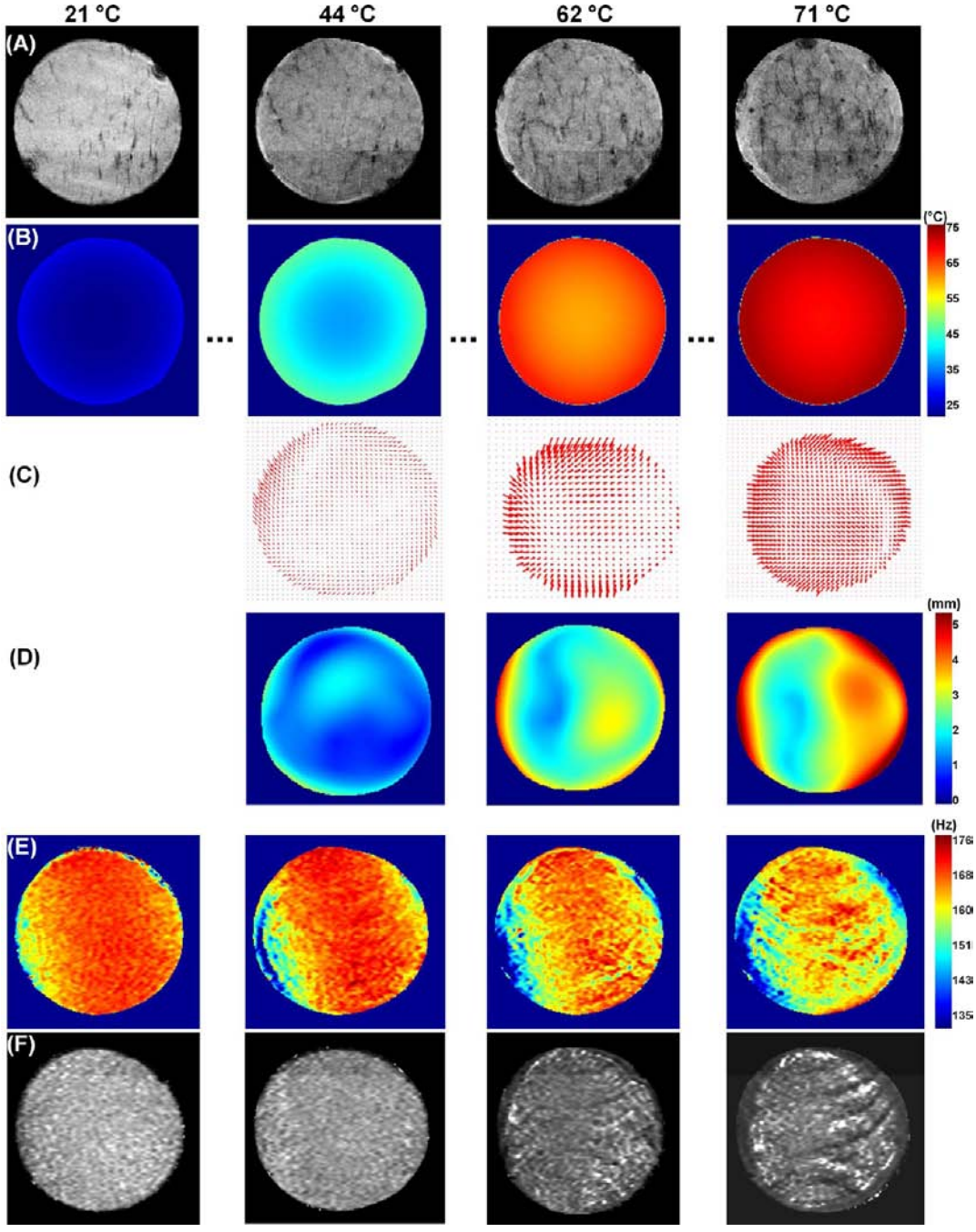

Figure 3. Sample with low IMCT content (slice 3/5). A) T_2*-weighted MR images (DIs). The windowing of gray levels was adjusted for each image to compensate for continuous SNR loss. (B) Corresponding temperature maps obtained by numerical simulation for four average temperatures in the sample. (C) Corresponding representations of deformation as a function of direction and magnitude calculated by nonlinear optimal registration from two consecutive DIs. (D) Corresponding representations of the magnitude of deformation calculated by nonlinear optimal registration from two consecutive DIs. (E) Corresponding B1 maps. (F) Corresponding proton density maps.

■ RESULTS AND DISCUSSION

Figures 2 and 3 show the different maps obtained at 4 average temperatures and in the central slice (3/5) of the sample for a high IMCT content sample and for a low IMCT content sample, respectively. They validate two important hypotheses: (i) DIs clearly show internal fiducial markers at each temperature despite the difficult experimental conditions leading to the continuous loss of SNR (Figures 2A and 3A), (ii) experimental B1 distribution is inhomogeneous in the sample and evolves with temperature (Figures 2E and 3E), and (iii) temperature is inhomogenously distributed and leads to significant spatial variation of both deformation and PD. Under these conditions, the spatial registration step converged whatever the temperature and resulted in a robust estimation of the deformation fields in direction and magnitude (Figures 2C,D and 3C,D). Figures 2E and 3E show the pertinence of this corrective mapping for PD as a function of temperature. Indeed, field B1 depends on several factors, notably the dimensions of the sample and its dielectric properties (permittivity and conductivity), resonance frequency, type,

dx.doi.org/10.1021/jf2046569 | J. Agric. Food Chem. 2012, 60, 4678–4687

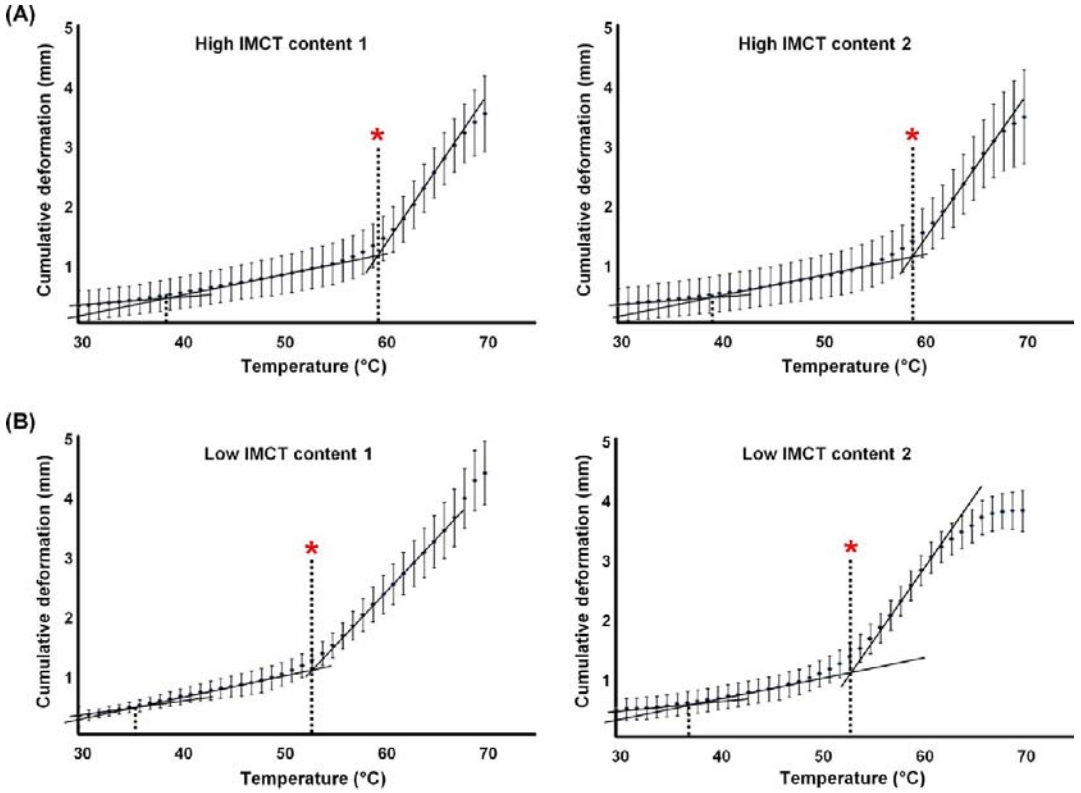

Figure 4. Cumulative deformation (mm) versus temperature (°C) for high (A) and low (B) IMCT content samples. Error bars represent the standard deviation. The red asterisks marks the inflection point.

and geometry of the coil used. This indicates moreover that the precise measurement in situ of the PD in MRI during heating must always be accompanied with a map of field B1 to take into account its evolution due to deformation and to variations of the sample's dielectric properties. Lastly, the resulting temperature, deformations, and transfers of water cannot be considered as homogeneous, emphasizing the advantage of in situ MRI to model phenomena.

For better visual inspection, it should be noted that the gray scale windowing was adjusted to compensate for SNR loss for the PD maps shown in Figures 2F and 3F.

Average Temperature-Courses of Deformation. High and low IMCT content samples presented similar deformation responses to thermal treatment. For both samples, deformation was greater at the surface than at the center of the sample because of the thermal gradient, the highest temperatures being on the external part of the sample. Cumulative deformation versus temperature (Figure 4) exhibits the same behavior for both samples: before 40 °C, cumulative deformation is very slight (0.01 mm/°C) and corresponds to the accumulation of the image registration error module during field deformation computation.[17] After this, a shallow slope can be observed before an inflection point (see red asterisks in Figure 4) marking a rise in the slope. The slopes are the same for the 4 samples: 0.030 ± 0.003 mm/°C before the inflection point and 0.21 ± 0.02 mm/°C after. Local information reveals a moderate strain between ∼38 °C and ∼55 °C. This phase corresponds to myosin denaturing, and the beginning of collagen denaturing,[30,31] explaining the slight deformation observed. During this phase, juice is essentially transferred to interfascicular spaces within the muscle.[16,32,33] The acceleration of deformation is due, on the one hand, to the heating of sarcoplasmic proteins,[34] leading to their denaturing, as reported in Hoult,[35] and therefore to a reduction of the mechanical resistance of the myofibers to a mechanical stress; however, the deformation is due to the contraction of collagen leading to mechanical constraints that in turn lead to the contraction of the connective network.[36] Water is then expelled to the exterior of the sample,[32] visible as a surrounding hypersignal in Figures 2A and 3A, which explains the strong deformation observed. Plateaus of deformations that occur from ∼68 °C can be explained by the end of one or several of these phenomena. Finally, the total (final) transverse deformation is the same whatever the IMCT content. This is consistent with the limitative characteristic of the muscle fiber's mechanical resistance to transverse contraction.[37]

Although our experiments were performed on only two samples per category (low IMCT and high IMCT contents), a significant difference of deformation was revealed between these categories. Nevertheless, our results are consistent for the five studied slices. The samples with little connective tissue presented accelerated deformation from 53 °C, whereas it occurs at a higher temperature, i.e., 58.5 °C, in samples with higher connective tissue content (Figure 4). This difference can first be explained by a difference in collagen type. Higher collagen content is often characteristic of older animals, whose degree of collagen reticulation and thus denaturation temperature increases.[38] This could also explain that at the end of cooking, more marked and earlier (65 °C) saturation of deformation was observed for the second sample with low IMCT content. The second assumption is the difference of denaturation temperature between the endomysium and the perimysium.[39] Denaturation of the endomysium at about 53 °C can cause measurable contraction only if there is little perimysium (Figure 4B). Otherwise, the latter prevents contraction by the

dx.doi.org/10.1021/jf2046569 | J. Agric. Food Chem. 2012, 60, 4678−4687

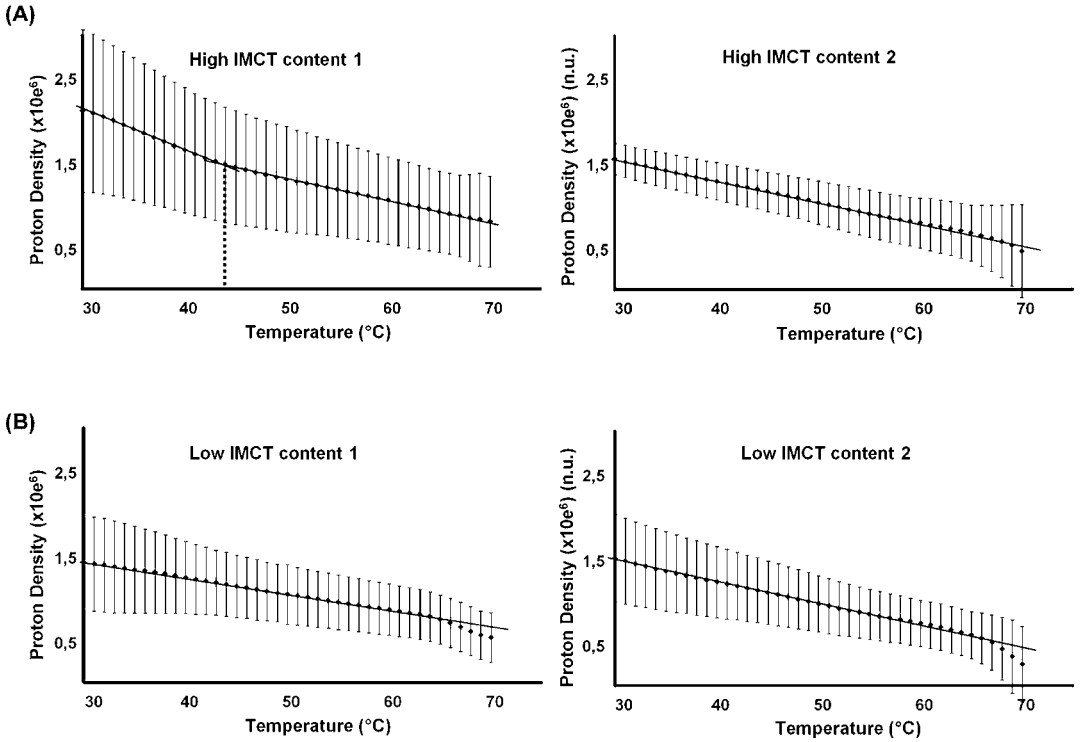

Figure 5. Proton density versus temperature (°C) for high (A) and low (B) IMCT content samples. Error bars represent the standard deviation.

endomysium by providing a protective sheath to the muscle up to 58 °C, which is the temperature of its own denaturation and the resulting contraction (Figure 4A). In addition, we observed (Figures 2A and 3A) that the deformation did not follow the same radial symmetry as temperature, emphasizing that factors other than temperature likely determine deformation, in particular structural factors, such as the distribution of IMCT. The hypothesis is that a high amount of connective tissue is expressed by greater heterogeneity of its distribution inducing anisotropic contraction. Conversely, when this amount is less, its distribution is homogeneous and contraction is more radial.

Average Temperature-Courses of Proton Density. As shown in Figure 5, the PD in the muscle decreases considerably with temperature. This decrease is consistent with that reported by Micklander[40] and Shaarani.[41] For three samples, we observed a linear loss of 2%/°C up to 65−67 °C, which then tended to be greater close to 70 °C, mainly in the case of low muscle IMTC. For the first sample containing a large amount of IMCT, two clear slopes could be observed, 4.7%/°C from 30 to 44 °C and 2.5%/°C from 44 to 70 °C. These losses lead to a reduction of total PD during cooking from 60 to 83% depending on the sample. This reduction is in part due to Curie's law that states that PD is inversely proportional to temperature,[42,43] i.e., corresponding to a signal change of 0.29%/°C to 0.34%/°C in our experimental range of 20−75 °C. The reduction of PD with temperature can also be explained by contraction that expels intramuscular water outside the muscle. This is undoubtedly the phenomenon that explains the sudden fall of PD when close to 70 °C for 3 of our samples. The quantification of final water loss[16,44] permits explaining approximately 40% of the reduction of PD.

Instead of a true PD map, we in fact measured the amplitude of magnetization present in each voxel of the sample. This amplitude was proportional not only to the density of the spins observed but also to the temperature, as shown by the decrease of PD measured as a function of temperature. Because the observation frequency was tuned to the resonance of water protons, the measured amplitude was therefore theoretically proportional to their density, i.e., water content.

The amplitude of magnetization was derived from two SE acquisitions differing by their echo times, from which only a single amplitude can be inferred. In general, this amplitude is a biased estimate of total water content since the ideal unbiased approach requires summing the amplitudes of all the water pools. However, when a single water pool dominates, as in muscle, the bias due to monoexponential modeling is low, provided T_2 of the bulk component remains higher than the lowest echo time.

The results of Bertram et al.[18] obtained by the reference nonlocalized NMR method show that there is no major redistribution of water pools when comparing distributions of T_2 relaxation times between raw and cooked pork meat at the same room temperature, and in situ during heating for a temperature range similar to ours. A bulk water pool remains that shifts slightly toward lower T_2. This is consistent with the results reported later on chicken meat[41] and with our previous findings[17] indicating a decrease of T_2, measured by a two-point imaging protocol. For all these studies, bulk T_2 was in the range from 20 to 80 ms, which remained higher than our lowest echo time (13 ms).

When heating a muscle to 76 °C and monitoring return to the initial temperature, Chen et al.[43] and Kovacsné et al.[45] showed that the evolution of PD with temperature is not reversible, contrary to what is observed in fat. The authors therefore conclude on an effect linked to the thermal modification of the constituents of the muscle since fat is not denatured at this temperature. Our results permit adding that transfers of water from intracellular spaces to interfascicular spaces, and then to the exterior of the muscle, also contribute to this irreversibility.

The sample high IMCT content 1 presented shrinkage of PD with temperature twice as fast below 44 °C. This phenomenon can likely be explained by the considerably higher PD of this

dx.doi.org/10.1021/jf2046569 | J. Agric. Food Chem. 2012, 60, 4678−4687

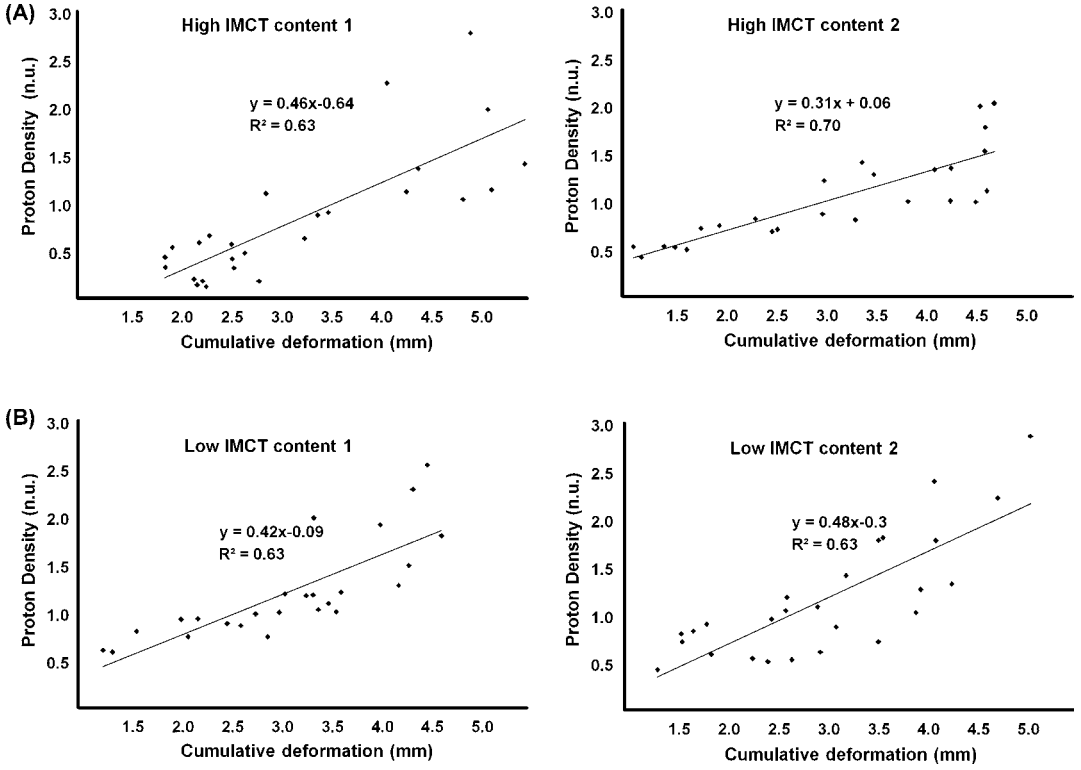

Figure 6. Proton density versus cumulative deformation (mm) for high (A) and low (B) IMCT content samples. These results are obtained on several ROIs taking on 5 slices of each sample on the last two acquisitions at high temperature.

sample before cooking, possibly resulting in a high loss of water.[44]

For all the samples, it should be noted that the large standard deviations reflect the noise propagated on the maps of PD (Figures 2F and 3F). In spite of all this, the very high number of voxels per slice (more than 10,000) endows statistic robustness to the averaged values presented.

Proton Density versus Cumulative Deformation. An original aspect of our approach is that it provides a direct and average relationship between deformation and quantity of water.

Figures 2 and 3 seem to show a correlation between the deformation modulus (line D) and the density of protons (line F) at high temperatures. A preliminary study has shown that there is no correlation between deformation and PD when comparing measurements voxel by voxel due to considerable spatial variations of PD (contrary to deformation). Part of this variability is moreover due to the presence of mobile water in the interfascicular spaces, which remains visible in spite of the effect of partial volume.[16] We therefore chose to average PD in ROIs in order to reduce this variability. This approach highlights the correlation coefficient of Spearman R^2 of the order 0.63 to 0.70 (Figure 6), which shows that the most deformed zones are those where PD is highest, which may seem counterintuitive, though consistent with the poroelastic theory.[46] This theory describes moisture transport using Darcy's law, which states that the fluid flow rate is linear with the pressure gradient. The pressure is partly due to the elasticity of the solid matrix of the porous material. It is fair to assume that the poroelastic theory also applies to meat during cooking, but in this case, it is supplemented with a constitutive equation for the pressure exerted by the contracting protein network during heating on the interstitial fluid.[47] In this study, the interpretation was based on Darcy's law: water migrates from a high pressure area to a low pressure area. In the case of meat cooking, because of muscle contractions, the pressure in the muscle becomes higher than the external pressure, thus causing water to transfer from the sample toward the exterior. Moreover, at the superficial area of the sample, the temperature is higher than at the center, leading to the creation of interfascicular channels that may trap the migrating water. It is worthwhile noting that our method is dynamical and thus gives instantaneous images of PD during the heating process, a feature for which there is no equivalent, while water content in cooking meat is classically studied at the end of the heating process.

Figure 6 shows for 3 of the 4 samples, an increase of PD of 0.45 (n.u.) per mm of cumulative deformation. The fourth seems to be less sensitive to deformation (0.31 n.u. per mm). The calculation of confidence intervals of 95% of the slopes of our four lines of correlation are 0.31−0.61, 0.22−0.39, 0.28−0.56, and 0.32−0.64 for the samples high IMCT content 1, high IMCT content 2, low IMCT content 1, and low IMCT content 2, respectively. These intervals overlap, meaning that the four models are not significantly different justifying merging the data in a global model presented in Figure 7. This global model confirms the positive relationship between cumulative deformation and proton density.

The effects of temperature on cumulative deformation and water content described here were reproducibly observed for four different samples of the same muscle type (BF). On the basis of the spatial information provided by our imaging methodology to intramuscular structural variability (e.g., size of fascicles) and to differences of temperature regime inside the sample, a single experiment provides extensive information for modeling the relationship between temperature and deformation. However, both interanimal variation and muscle type are likely to have important effects, which deserve further studies on different muscle types, from different animals.

dx.doi.org/10.1021/jf2046569 | J. Agric. Food Chem. 2012, 60, 4678−4687

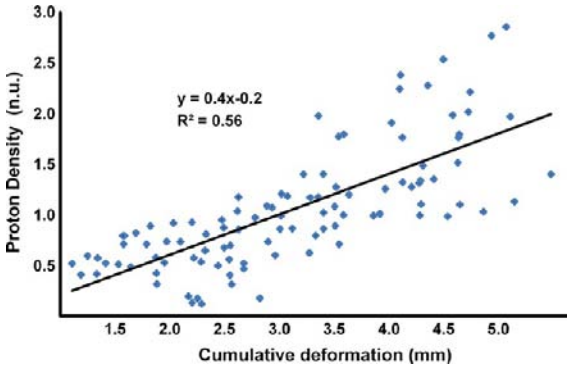

Figure 7. Proton density versus cumulative deformation (mm) for merged data. These results are obtained on several ROIs taking on 5 slices of each sample on the last two acquisitions at high temperature.

Indeed, our method can be generalized provided that muscles sufficiently rich in elastin are used, as they guarantee good contrast of T_2*-weighted MRI.

Whatever the case, the works presented here are pioneering in that they focus on the simultaneous presentation of deformation maps, water content, and temperature during cooking. They should permit even better understanding of the occurrence of denaturation phenomena and contraction as a function of the type and state of proteins. Nonetheless, we admit that our cooking method is slower than that used in reality, as this slow gradient was chosen to highlight all the phenomena, despite the time resolution of the MRI.

In addition to the map of water content, information on its local diffusivity would help in interpreting water transfers observed at different scales during cooking. To take this understanding still further, it will be necessary to associate biochemical and spectroscopic analyses to know the nature and structural state of sarcoplasmic, myofibrillar, and collagen proteins present in each of the samples analyzed by MRI. More thorough modeling of the link between mechanical constraints and transfers of water should also permit improving the interpretation of the phenomena studied.

Better knowledge of the mechanisms responsible for the transfer of juice during cooking will permit better quantification of the fate, in the food, of hydrosoluble micronutrients since some of these micronutrients, such as iron and vitamins of group B, are very present and bioavailable in meats, especially beef. The fact of being able to study simultaneously water transfer and mechanical constraints will also lead to better understanding of the link between the tenderness and juiciness of meats. Since, in a general way, the reaction kinetics involved depend on the concentration of water, this work will permit better understanding of the sequence of all the biochemical reactions responsible for the quality of cooked meat.

In the framework of developing industrial cooking, it would be possible to study the effect of mechanical prestressing, mainly that exerted during maturation, on deformation in cooking, another issue of interest to industry. The role of ingredients is also fundamental, for example, the effects of salting on cooking are of interest for the pork processing industry. Lastly, in situ monitoring of structural changes during cooking should be applied to all foods for which cooking is the decisive parameter for final quality.

AUTHOR INFORMATION

Corresponding Author

*Phone: 33-4-73-62-45-93. Fax: 33-4-73-62-40-89. E-mail: sylvie.clerjon@clermont.inra.fr.

Funding Sources

This work has received a grant from the E.U. project ProSafeBeef.

Notes

The authors declare no competing financial interest.

ACKNOWLEDGMENTS

The MRI experiments were performed at the biological systems MR platform at the INRA center of Clermont-Ferrand, France (www.clermont.inra.fr/rmsb/).

ABBREVIATIONS USED

BF, *biceps femoris*; B1, amplitude of the active emission RF field; DI, deformation image; EPI, echo planar imaging; FOV, field of view; GE, gradient-echo; INRA, Institut National de la Recherche Agronomique; IMCT, intramuscular connective tissue; MRI, magnetic resonance imaging; PD, proton density; POCS, projection onto convex sets; RF, radiofrequency; ROI, regions of interest; SE, spin echo; SNR, signal to noise ratio; TE, echo-time; TR, repetition time; T2, transverse (or spin−spin) relaxation time; T2*-weighted, susceptibility-weighted; 2D, bidimensional

REFERENCES

(1) Jeremiah, L. E.; Gibson, L. L.; Aalhus, J. L.; Dugan, M. E. R. Assessment of palatability attributes of the major beef muscles. *Meat Sci.* **2003**, *65*, 949−958.

(2) Harris, J. M.; Rhodes, D. N.; Chrystall, B. B. Meat texture: I. Subjective assessment of the texture of cooked beef. *J. Sci. Food Agric.* **1972**, *3*, 101−114.

(3) Becker, T. Consumer perceptions of fresh meat quality: A framework for analysis. *Brit. Food J.* **2000**, *102*, 158−176.

(4) Dransfield, E.; Francombe, M. A.; Whelehan, O. P. Relationships between sensory attributes in cooked meat. *J. Texture Stud.* **1984**, *15*, 33−48.

(5) Tornberg, E. Effects of heat on meat proteins—Implications on structure and quality of meat products. *Meat Sci.* **2005**, *70*, 493−508.

(6) Yven, C.; Culioli, J.; Mioche, L. Meat bolus properties in relation with meat texture and chewing context. *Meat Sci.* **2005**, *70*, 365−371.

(7) Bouton, P. E.; Harris, P. V. The effects of cooking temperature and time on some mechanical properties of meat. *J. Food Sci.* **1972**, *37*, 140−144.

(8) Honikel, K. O. Reference methods for the assessment of physical characteristics of meat. *Meat Sci.* **1998**, *49*, 447−457.

(9) Brunton, N. P.; Lyng, J. G.; Zhang, L.; Jacquier, J. C. The use of dielectric properties and other physical analyses for assessing protein denaturation in beef *biceps femoris* muscle during cooking from 5 to 85 °C. *Meat Sci.* **2006**, *72*, 236−244.

(10) Zheng, C.; Sun, D. W.; Zheng, L. Correlating colour to moisture content of large cooked beef joints by computer vision. *J. Food Eng.* **2006**, *77*, 858−863.

(11) Du, C. J.; Sun, D. W. Correlating shrinkage with yield, water content and texture of pork ham by computer vision. *J. Food Process Eng.* **2005**, *28*, 219−232.

(12) Ghosh, P. K.; Jayas, D. S.; Gruwel, M. L. H.; White, N. D. G. Magnetic resonance image analysis to explain moisture movement during wheat drying. *Am. Soc. Agric. Biol. Eng.* **2006**, *49*, 1181−1191.

(13) Hills, B. Food processing: An MRI perspective. *Trends Food Sci. Technol.* **1995**, *6*, 111−116.

(14) Ruiz-Cabrera, M. A.; Foucat, L.; Bonny, J.-M.; Renou, J. P.; Daudin, J. D. Assessment of water diffusivity in gelatin gel from moisture profiles. I—Non-destructive measurement of 1D moisture profiles during drying from 2D nuclear magnetic resonance images. *J. Food Eng.* **2005**, *68*, 209−219.

(15) Mohoric, A.; Vergeldt, F.; Gerkema, E.; Van Dalen, G.; Van den Doel, L. R.; Van Vliet, L. J.; Van Ad, H.; Van Duynhoven., J. The effect

of rice kernel microstructure on cooking behavior: a combined μ-CT and MRI study. *Food Chem.* **2009**, *115*, 1491−1499.
(16) Bouhrara, M.; Clerjon, S.; Damez, J.-L.; Chevarin, C.; Portanguen, S.; Kondjoyan., A.; Bonny, J.-M. Dynamic MRI and thermal simulation to interpret deformation and water transfer in meat during heating. *J. Agric. Food Chem.* **2011**, *59*, 1229−1235.
(17) Bouhrara, M.; Lehallier, B.; Clerjon, C.; Damez, J.-L.; Bonny, J.-M. Mapping of muscle deformation during heating: in situ dynamic MRI and nonlinear registration. *Magn. Reson. Imaging* **2012**, *30*, 422−430.
(18) Bertram, H. C.; Engelsen, S. B.; Busk, H.; Karlson, A. H.; Andersen, H. J. Water properties during cooking of pork studied by low-fiel NMR relaxation: Effects of curing and the RN^{-}gene. *Meat Sci.* **2004**, *66*, 437−446.
(19) Finsterbusch, J.; Frahm, J. Half-Fourier single-shot STEAM MRI. *Magn. Reson. Med.* **2002**, *47*, 611−615.
(20) Haacke, E. M.; Lindskog, E. D.; Lin, W. A fast, iterative, partial-Fourier technique capable of local phase recovery. *J. Magn. Reson.* **1991**, *92*, 126−145.
(21) Tawara, N.; Nitta, O.; Kuruma, H.; Niitsu, M.; Itoh, A. T_2 mapping of muscle activity using ultrafast imaging. *Magn. Reson. Med. Sci.* **2011**, *10*, 85−91.
(22) Simmons, A.; Tofts, P. S.; Barker, G. J.; Arridge, S. R. Sources of intensity nonuniformity in spin echo images at 1.5 T. *Magn. Reson. Med.* **1994**, *32*, 121−128.
(23) Alecci, M.; Collins, C. M.; Smith, M. B.; Jezzard, P. Radio frequency magnetic field mapping of a 3 T birdcage coil: Experimental and theoretical dependence on sample properties. *Magn. Reson. Med.* **2001**, *46*, 370−385.
(24) Zhuang, H.; Nelson, S. O.; Trabelsi, S.; Savage, E. M. Dielectric properties of uncooked chicken breast muscles from ten to one thousand eight hundred megahertz. *Poultry Sci.* **2007**, *86*, 2433−2440.
(25) Sipahioglu, O.; Barringer, S. A.; Taub, I.; Prakash, A. Modeling the dielectric properties of ham as function of temperature and composition. *J. Food Sci.* **2003**, *68*, 904−909.
(26) Stollberger, R.; Wach, P. Imaging of the active B1 field in vivo. *Magn. Reson. Med.* **1996**, *35*, 246−251.
(27) Bouhrara, M.; Bonny, J.-M. B1 mapping with selective pulses. *Magn. Reson. Med.* **2012**, DOI: 10.1002/mrm.24146.
(28) Woods, R. P.; Grafton, S. T.; Holmes, C. J.; Cherry, S. R.; Mazziotta, J. C. Automated image registration: I. General methods and intrasubject, intramodality validation. *J. Comput. Assist. Tomogr.* **1998**, *22*, 139−152.
(29) Woods, R. P.; Grafton, S. T.; Holmes, C. J.; Cherry, S. R.; Mazziotta, J. C. Automated image registration: II. Intersubject validation of linear and nonlinear models. *J. Comput. Assist. Tomogr.* **1998**, *22*, 153−165.
(30) Martens, H.; Stabursvik, E.; Martens, M. Texture and colour changes in meat during cooking related to thermal denaturation of muscle proteins. *J. Texture Stud.* **1982**, *13*, 291−309.
(31) Hindman, J. C. Proton resonance shift of water in the gas and liquid states. *J. Chem. Phys.* **1966**, *44*, 4582−4592.
(32) Christensen, M.; Purslow, P. P.; Larsen, L. M. The effect of cooking temperature on mechanical properties of whole meat, single muscle fibres and perimysial connective tissue. *Meat Sci.* **2000**, *55*, 301−307.
(33) Straadt, I. K.; Rasmussen, M.; Andersen, H. J.; Bertram, H. C. Aging-induced changes in microstructure and water distribution in fresh and cooked pork in relation to water-holding capacity and cooking loss—A combined confocal laser scanning microscopy (CLSM) and low-field nuclear magnetic resonance relaxation study. *Meat Sci.* **2007**, *75*, 687−695.
(34) Nikmaram, P.; Yarmand, M. S.; Emamjomeh, Z.; Darehabi, H. K. The effect of cooking methods on textural and microstructure properties of Veal muscle. *Global Vet.* **2011**, *6*, 201−207.
(35) Hoult, D. I.; Lauterbur, P. C. The sensitivity of the zeugmatographic experiment involving human samples. *J. Magn. Reson.* **1979**, *34*, 425−433.
(36) Darrasse, L.; Ginefri, J. C. Perspectives with cryogenic RF probes in biomedical MRI. *Biochimie* **2003**, *85*, 915−937.
(37) Lepetit, J. A theoretical approach of the relationships between collagen content, collagen cross-links and meat tenderness. *Meat Sci.* **2007**, *76*, 147−159.
(38) Horgan, D. J.; Jones, P. N.; King, N. L.; Kurth, L. B.; Kuypers, R. The relationship between animal age and the thermal stability and cross-link content of collagen from five goat muscles. *Meat Sci.* **1991**, *29*, 251−262.
(39) Li, C. B.; Zhou, G. H.; Xu, X. L. Dynamical changes of beef intramuscular connective tissue and muscle fiber during heating and their effects on beef shear force. *Food Bioprocess Technol.* **2010**, *3*, 521−527.
(40) Micklander, E.; Peshlov, B.; Purslow, P. P.; Engelsen, S. B. NMR-cooking: Monitoring the changes in meat during cooking by low-field H-1-NMR. *Trends Food Sci. Technol.* **2002**, *13*, 341−346.
(41) Shaarani, S. M.; Nott, K. P.; Hall, L. D. Combination of NMR and MRI quantitation of structure and structure changes for convection cooking of fresh chicken meat. *Meat Sci.* **2006**, *72*, 398−403.
(42) Abragam, A. *The Principles of the Nuclear Magnetism*; Oxford University Press: New York City, 1983; p 599.
(43) Chen, J.; Bruce, L.; Pauly, K. B. Investigation of proton density for measuring tissue temperature. *J. Magn. Reson. Imaging* **2006**, *23*, 430−434.
(44) Oillic, S.; Lemoine, E.; Gros, J. B.; Kondjoyan, A. Kinetic analysis of cooking losses from beef and other animal muscles heated in a water bath—Effect of sample dimensions and prior freezing and ageing. *Meat Sci.* **2011**, *88*, 338−346.
(45) Kovacsne Oroszvari, B.; Bayod, E.; Sjoholm, I.; Tornberg, E. The mechanisms controlling heat and mass transfer on frying of beefburgers. III. Mass transfer evolution during frying. *J. Food Eng.* **2006**, *76*, 169−178.
(46) Barriere, B.; Leibler, L. Kinetics of solvent absorption and permeation through a highly swellable elastomeric network. *J. Polym. Sci., Polym. Phys.* **2003**, *41*, 166−182.
(47) Van der Sman, R. G. M. Moisture transport during cooking of meat: An analysis based on Flory−Rehner theory. *Meat Sci.* **2007**, *76*, 730−738.